Supporting Information for

Integrated terahertz generator-manipulator using epsilon-near-zero-hybrid nonlinear metasurfaces

Yongchang Lu[†, ¶, ‡], Xi Feng[†, ¶, ‡], Qingwei Wang[†, ¶, ‡], Xueqian Zhang[†,*], Ming Fang[§,*], Wei E.I. Sha[‖], Zhixiang Huang[§], Quan Xu[†], Li Niu[†], Xieyu Chen[†], Chunmei Ouyang[†],Yuanmu Yang[⊥], Xixiang Zhang[¶], Eric Plum[#], Shuang Zhang[††,*], Jiaguang Han[†,*], Weili Zhang[‡‡]

[†]Center for Terahertz waves and College of Precision Instrument and Optoelectronics Engineering, Tianjin University and the Key Laboratory of Optoelectronics Information and Technology (Ministry of Education), Tianjin 300072, China.

[§]Key Laboratory of Intelligent Computing and Signal Processing, Ministry of Education, Anhui University, Hefei 230039, China

[‖]Key Laboratory of Micro-nano Electronic Devices and Smart Systems of Zhejiang Province, College of Information Science & Electronic Engineering, Zhejiang University, Hangzhou 310027, China

[⊥]State Key Laboratory of Precision Measurement Technology and Instruments, Department of Precision Instrument, Tsinghua University, Beijing 100084, China

[¶]Physical Science and Engineering Division, King Abdullah University of Science and Technology (KAUST), Thuwal 23955-6900, Saudi Arabia

[#]Optoelectronics Research Centre and Centre for Photonic Metamaterials, University of Southampton, Highfield, Southampton SO17 1BJ, UK

[††]Department of Physics, Faculty of Science, University of Hong Kong, Hong Kang

[‡‡]School of Electrical and Computer Engineering, Oklahoma State University, Stillwater, Oklahoma 74078, USA.

[‡]These authors contributed equally to this work

[*]Corresponding authors. Email: alearn1988@tju.edu.cn (XQ. Zhang), mingfang@ahu.edu.cn (M. Fang), shuzhang@hku.hk (S. Zhang), jiaghan@tju.edu.cn (J. Han)

KEYWORDS: Terahertz, integrated generator-manipulator, metasurface, epsilon-near-zero, nonlinear Pancharatnam-Berry phase

Note 1. Theoretical fitting of the transmission spectra

The Fano-like transmission spectrum under *x*-polarized illumination in Figure 2c can be regarded as the plasmon-induced transparency effect and can be described by coupled-mode theory (CMT)

$$\begin{cases} \dfrac{1}{2\pi}\dfrac{\partial}{\partial t}\begin{pmatrix} a_b \\ a_d \end{pmatrix} = \begin{pmatrix} if_b - \gamma_b - \gamma_b' & i\chi \\ i\chi & if_d - \gamma_d - \gamma_d' \end{pmatrix}\begin{pmatrix} a_b \\ a_d \end{pmatrix} + i\begin{pmatrix} d_{1b} & d_{2b} \\ d_{1d} & d_{2d} \end{pmatrix}\begin{pmatrix} S_1^+ \\ S_2^+ \end{pmatrix} \\ \begin{pmatrix} S_1^- \\ S_2^- \end{pmatrix} = \begin{pmatrix} S_{11} & S_{12} \\ S_{21} & S_{22} \end{pmatrix}\begin{pmatrix} S_1^+ \\ S_2^+ \end{pmatrix} + i\begin{pmatrix} d_{1b} & d_{1d} \\ d_{2b} & d_{2d} \end{pmatrix}\begin{pmatrix} a_b \\ a_d \end{pmatrix} \end{cases}, \tag{S1}$$

where $a_{b,d}$, $f_{b,d}$, $\gamma_{b,d}$, and $\gamma'_{b,d}$ depict the complex resonance amplitude, resonance frequency, radiation loss rate, and absorption loss rate with the subscript *b* and *d* representing the bright mode (magnetic resonance mode of the SRR) and the dark mode (lossy ENZ mode of the ITO film), respectively; χ depicts the coupling strength between the bright mode and the dark mode, S_1^+ and S_2^+ depict the inputs from the structure side (port 1) and the substrate side (port 2), while S_1^- and S_2^- depict the outputs from the port 1 and port 2; d_{ij} depicts the excitation strength between the input and the resonance modes with i = 1, 2 and j = *b*, *d*; S_{ij} depicts the *S*-parameter between the inputs and outputs in the absence of the SRR and ITO film.

Here, the system is excited merely from the structure side, hence $S_2^+ = 0$. Meanwhile, the lossy ENZ mode of the ITO film is a dark mode under normal illumination, which is nonradiative and cannot be directly excited by the external field, thus $\gamma_d = d_{1d} = d_{2d} = 0$. According to time-inversion symmetry and energy conservation law, we have $|d_{1b}|^2 + |d_{2b}|^2 = 2\gamma_b$ and $d_{2b} = \eta d_{1b}$, where $\eta = n^{1/2}$ describes the asymmetry of the modes' radiations toward the two sides due to the presence of the quartz substrate with n = 1.44 being the refractive index of the substrate[1]. For such a quartz substrate, $S_{11} = (1 - n)/(1 + n)$, $S_{12} = S_{21} = 2n^{1/2}/(1 + n)$, and $S_{22} = (n - 1)/(1 + n)$. By solving Eq.

(S1), the reflection and transmission coefficients can be calculated as:

$$r = \frac{S_1^-}{S_1^+} = S_{11} - \frac{d_{1b}^2 \times \left[i\left(f - f_d\right) + \gamma_d' \right]}{\left[i\left(f - f_b\right) + \gamma_b + \gamma_b' \right] \times \left[i\left(f - f_d\right) + \gamma_d' \right] + \chi^2}, \tag{S2}$$

$$t = \frac{S_2^-}{S_1^+} = S_{21} - \frac{\eta \times d_{1b}^2 \times \left[i\left(f - f_d\right) + \gamma_d' \right]}{\left[i\left(f - f_b\right) + \gamma_b + \gamma_b' \right] \times \left[i\left(f - f_d\right) + \gamma_d' \right] + \chi^2}. \tag{S3}$$

respectively. Here, f depicts the frequency. Figure S1a illustrates the fitted result of the measured transmission spectrum in Figure 2d under the x-polarized illumination using Eq. (S3), where great agreement is achieved. When χ = 0, Eq. (S3) depicts the transmission without the dark mode, namely, the transmission of the SRR metasurface. Figure S1b illustrates the corresponding fitted result, which shows a considerable similarity with the measured transmission spectrum in Figure 2c under x-polarized illumination. The frequency shift can be attributed to the fabrication deviation since the SRR metasurface was directly patterned on a glass substrate without the ITO film.

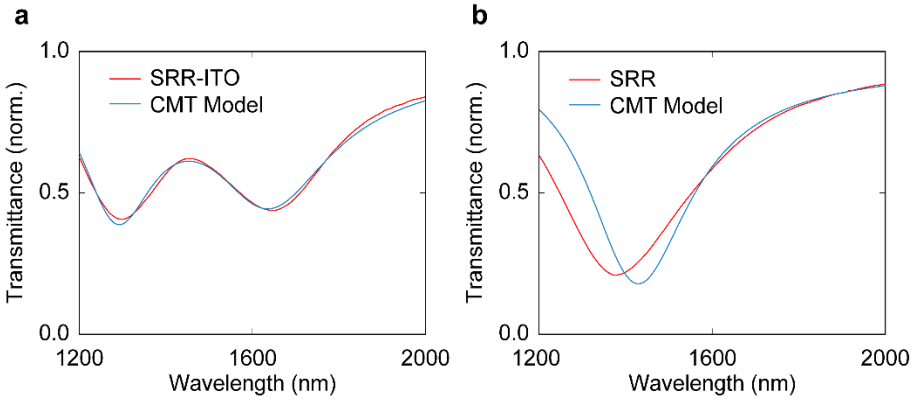

Figure S1. (a) Measured and fitted transmission spectra of the SRR-ITO metasurface under the x-polarized illumination, where the fitted parameters in CMT are f_b = 209.9 THz, γ_b = 12.2 THz, γ'_b = 9.2 THz, f_d = 205.4 THz, γ'_d = 16.8 THz, and χ = 25.1 THz, respectively. (b) Measured and fitted transmission spectra of the SRR metasurface under the x-polarized illumination, where the fitted parameters are the same as (a) but χ = 0 THz.

Note 2. Resonance features of the SRR-ITO metasurface

2.1. *Magnetic resonance of the SRR-ITO metasurface under the x-polarized illumination*

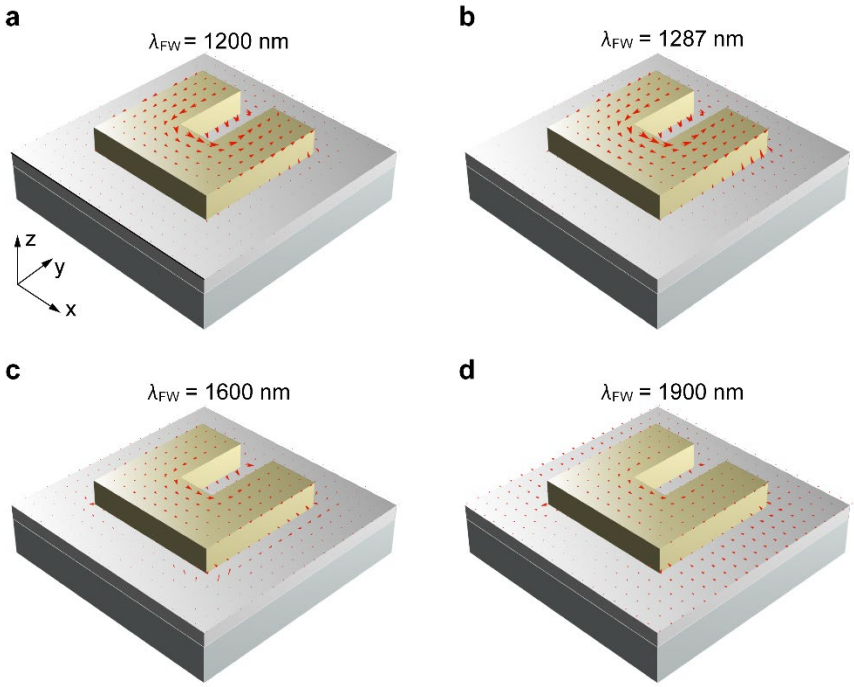

Figure S2. Simulated surface current distributions of the SRR-ITO metasurface at both the SRR and ITO surfaces under *x*-polarized illumination with FW wavelengths of 1200 nm (a), 1287 nm (b), 1600 nm (c) and 1900 nm (d), respectively.

Figure S2 illustrates the simulated surface current distributions of the SRR-ITO meta-atom at four different FW wavelengths of 1200 nm (a), 1287 nm (b), 1600 nm (c) and 1900 nm (d), respectively, under the *x*-polarized illumination. These four wavelengths are just across the resonance range of the SRR-ITO metasurface in Figure 2d. It can be seen that all these distributions have circulating surface currents on the SRR, which indicates that a magnetic dipole current distribution is excited over a wide band, although there is a resonance splitting effect owing to the coupling between the

SRR and the ITO film. At the SRR-ITO interface, especially in the contact areas, the surface currents contain normal components, which are induced by the enhanced normal electric field component at the interface that drives the movement of the free electrons.

2.2. *The weak resonance of the SRR-ITO metasurface under the y-polarized illumination*

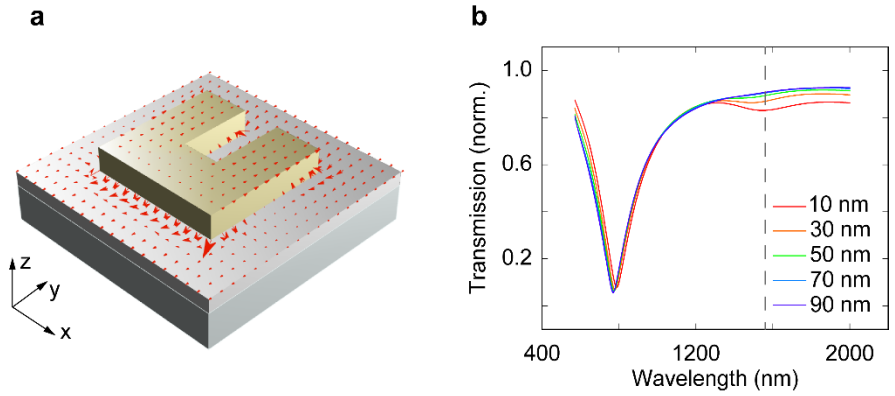

Figure S3. (a) Simulated surface current distributions of the SRR-ITO metasurface at both the SRR and ITO surfaces under *y*-polarized illumination with a FW wavelength of 1560 nm. (b) Simulated transmission spectra of the SRR-SiO_2-ITO metasurface with varying SiO_2 thickness. The dashed line marks the weak resonance dip around 1560 nm.

Similar to the measured result in Figure 2d, a weak resonance dip around 1560 nm was also observed in the simulated transmission spectra under *y*-polarized illumination. Figure S3a illustrates the corresponding simulated surface current distribution at the resonance wavelength. It is seen that it is an electric-dipole-like resonance, which can be attributed to the coupling effect between the electric resonance of the SRR and the ENZ mode of the ITO film under the *y*-polarized illumination. To clarify this, a silica interlayer was sandwiched between the SRR and the ITO film.

Here, we denoted it as an SRR-SiO_2-ITO metasurface. Figure S3b illustrates the simulated transmission spectra of the SRR-SiO_2-ITO metasurface with different thicknesses of the interlayer under *y*-polarized illumination. Clear electric dipole resonances are observed at ~800 nm for all the cases. The resonances around 1560 nm are within the side band area and far away compared to the resonance linewidth, causing them to become very weak. As the thickness of the interlayer increases, the coupling strength between the SRR and the ITO film gradually decreases and the weak resonance thus gradually disappears.

Note 3. Experimental measurements

3.1. *Basic experimental setup*

All the measurement results in the main text were measured using a home-made THz time-domain spectroscopy (TDS) system. The experimental setup is schematically illustrated in Figure S4. A Ti:Sapphire femtosecond laser amplifier (Coherent, Legend Elite Duo) was used as the laser source of the TDS system. The output amplified laser pulse has a central wavelength of 800 nm, pulse duration of 35 fs, and a repetition rate of 1.0 kHz. It was split into a generation beam and a detection beam by a beam splitter (BS) for driving the TDS system. The generation beam was injected into an optical parameter amplifier (OPA, Coherent OperA Solo) to generate a NIR femtosecond laser beam, whose central wavelength can be tuned from 1160 nm to 2000 nm with ~60 fs pulse duration. After passing through an optical chopper (370-Hz reference frequency), a neutral density (ND) filter, a broadband half-wave plate (HWP), and a NIR polarizer (P0) in sequence, this NIR beam was then loosely focused onto the samples located at the focus of the 90° off-axial parabolic mirror (PM1, 2" diameter, 2" focal length) by a convex lens (L3, 150-mm focal length). The generated THz beam was collimated by PM1 and then collected and focused by another parabolic mirror (PM2, 2" diameter, 4" focal length) to a detection ZnTe crystal (1-mm thickness, 110-cut). These two parabolic mirrors were arranged to compose a 4*f* system. The residual NIR laser was filtered out by a piece of paper (Filter) after the samples. The samples and the detection ZnTe crystal were placed on the focal plane of PM1 and PM2, respectively, to maximize the THz collection and detection efficiency. Between the PM2 and the detection ZnTe crystal, a 2 mm-thick silicon wafer was inserted, which functioned as a dichroic mirror, allowing the transmission of the THz beam

and the reflection of the detection beam. The detection beam separated from the amplified laser pulse by the BS was firstly guided into a delay line, which was used to change the relative optical time delay to the THz pulse. Then, the detection beam was attenuated by another ND and reflected onto the detection ZnTe crystal in the same path as the THz beam by the silicon wafer. Due to the electro-optical effect of the ZnTe crystal induced by the THz electric field, the polarization state of the detection beam was changed from linear polarization to slightly elliptical polarization. Before this electro-optical interaction, a 4*f* system consisting of two convex lenses L4 and L5 was introduced into the detection beam with a variable iris diaphragm (ID) placed at the front focal plane of L4 and with the back focal plane of L5 coinciding with the position of the detection ZnTe crystal. By leveraging the non-diffraction property of the 4*f* system at its conjugate planes, the spot size of the detection beam inside the detection ZnTe crystal can be freely adjusted by changing the aperture size of the ID. After transmission through a quarter-wave plate (QWP) and a Wollaston prism (WP), the detection beam was divided into two separate components with orthogonal polarization states. At last, they illuminated onto a balanced detector (BD). As a result, a voltage signal corresponding to the intensity difference of the two components was recorded by a lock-in amplifier (not shown), which is propotional to the applied THz field amplitude. By gradually changing the optical time delay, the THz time-domain pulse was measured.

For measuring the broadband THz generation results in Figure 3, the pump fluence was controlled by the ND, the polarization state of the NIR pump laser was controlled by the HWP and the P0, and the convex lens L3 was placed ~50 mm before the samples. The measured diameter of the NIR laser spot at the sample plane was ~1.1 mm, the optical chopping frequency was 370 Hz,

the integration time of the lock-in amplifier was 300 ms, and the scanning resolution of the time delay was 0.02 ps. The rotation angles of the detection ZnTe crystal, QWP, and the WP are all optimized following the previous literature[2,3].

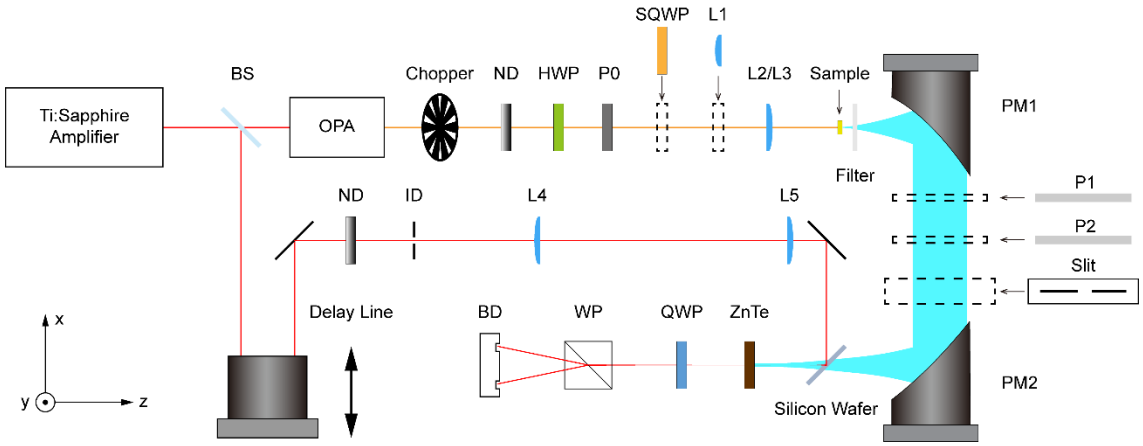

Figure S4. Experimental setup.

3.2. *Polarization-resolved measurements of the THz generation from the SRR-ITO metasurface*

To characterize the polarization properties of the THz generation from the SRR-ITO metasurface, we measured both the THz polarization state under *x*-polarized pumping (see Figure S5a) and the pump-polarization-dependent THz peak-to-peak amplitudes (see Figure S5b). In both cases, the pump wavelengths were 1360 nm, and the pump fluences were 147.3 μJ cm^{-2}. In Figure S5a, the THz peak-to-peak amplitudes were measured by changing the rotation angle β_1 of the THz linear polarizer P1 (see Figure S4, also P_{THz} in the inset of Figure S5a) while fixing the rotation angle of the other THz polarizer P2 (see Figure S4). Here, P2 was set to allow the transmission of only the *y*-polarized THz wave. It is seen that the measured THz peak-to-peak amplitudes (blue squares) well fits the $\cos^2(\beta_1)$ function (blue line), indicating that the THz waves are basically *y*-polarized. In Figure S5b, the FW polarization was controlled by the broadband NIR half wave plate HWP

and the broadband NIR polarizer P0 (see Figure S4), while both P1 and P2 were set to allow the transmission of only the *y*-polarized THz wave, $E_{THz,y}$. It can be seen that the measured THz peak-to-peak amplitudes (red dots) fit the $\sin^2(\beta_2)$ function (red line), indicating that *x*-polarized pumping – which excites the magnetic dipole resonance of the SRR – is most efficient.

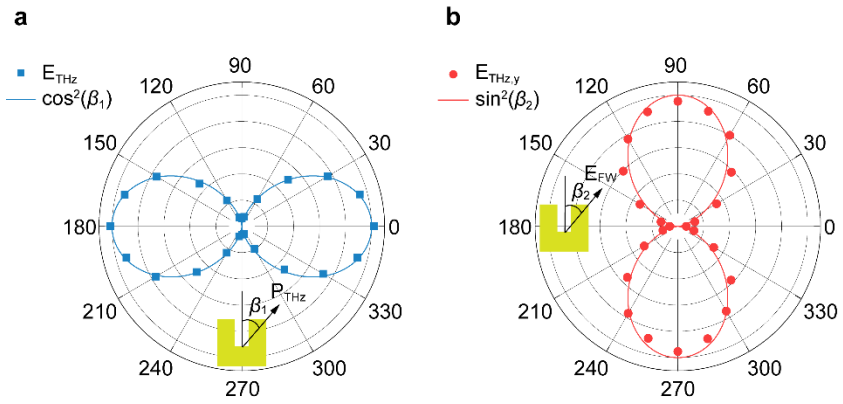

Figure S5. (a) Measured THz polarization state generated by the SRR-ITO metasurface under *x*-polarized pumping. (b) Measured pump-polarization-dependent THz peak-to-peak amplitudes generated by the SRR-ITO metasurface. A normally incident pump beam of 1360 nm wavelength was used in both cases. Angles are measured relative to the SRR's line of symmetry (*y*-axis).

3.3. *Measurements of the angle-resolved CP THz IGM*

In these measurements, the NIR pump beam size was expanded using a lens group composed of a convex lenses L1 (50-mm focus length) and L2 (100-mm focus length) to cover the angle-resolved CP THz IGM (IGM1). A super achromatic quarter-wave plate (SQWP) was inserted after polarizer P0 to realize RCP and LCP NIR pumps. IGM1 was placed with the nonlinear PB phase gradient along the *y* direction. Thus, the emitted CP THz wave was separated symmetrically with regard to the center *x*-*z* plane of the parabolic mirrors. Such a configuration ensured the same collection efficiency for the RCP and LCP THz waves. Two THz linear polarizers P1 and P2, and a 5-mm slit

mounted on a motorized translation stage were inserted between PM1 and PM2. To resolve the RCP and LCP components of the emitted THz wave, the transmission axis of P1 was rotated to be +45° and −45°, respectively, while that of P2 was fixed to be 0° (along *y*) to keep the same detection efficiency of the +45°- and −45°-polarized THz wave passing through P1. After that, the measured results were transformed into those in the circular polarization basis. By gradually moving the slit along the *y* direction, the emitted THz beam at different positions was detected step by step. Then, the *y* positions were converted to the emission angles considering the reflection by PM1 and plotted in Figure 6. Owing to the limited numerical aperture of PM1, only THz waves with absolute emission angles smaller than 26.6° can be collected.

3.4. *Measurements of the CP-dependent vortex THz IGM*

In these measurements, the RCP and LCP NIR pumps were also achieved by inserting a SQWP after polarizer P0, the CP-dependent vortex THz IGM (IGM2) was loaded onto a two-dimensional (2D) scanner which was a motorized 2D translation stage. Under CP normal pumping, the wavefronts of emitted THz waves were imaged onto the detection ZnTe crystal by the two parabolic mirrors. By raster scanning the position of IGM2 in the *x*-*y* plane, the THz wavefront at the detection ZnTe crystal also moved accordingly, thus the detection beam could interact with the THz fields at each position of the THz wavefront, allowing mapping of the THz wavefront. To respectively resolve the wavefronts of the emitted RCP and LCP THz waves, the same method as in Section 3 was applied (with the slit removed). IGM2 was translated in setps of 0.075mm.

Note 4: Simulations of the enhanced THz generation

4.1. *Simulation theory and parameters*

The linear and nonlinear interaction of the electromagnetic fields with the free electrons in the plasmonic structures can be given by

$$\nabla \times \mathbf{H} = \varepsilon_0 \frac{\partial \mathbf{E}}{\partial t} + \frac{\partial \mathbf{P}}{\partial t}, \tag{S4}$$

$$\nabla \times \mathbf{E} = -\mu_0 \frac{\partial \mathbf{H}}{\partial t}, \tag{S5}$$

$$\frac{\partial \boldsymbol{v}}{\partial t} + (\boldsymbol{v} \cdot \nabla)\boldsymbol{v} = -\frac{e}{m_e}(\mathbf{E} + \mu_0 \boldsymbol{v} \times \mathbf{H}) - \gamma \boldsymbol{v} - \frac{\nabla p}{n}, \tag{S6}$$

$$\frac{\partial n}{\partial t} = -\nabla \cdot (n\boldsymbol{v}), \tag{S7}$$

where Eqs. (S4) and (S5) are the Maxwell's equations that describe the propagation of the incident field, and the scattered field generated from electron motion; Eqs. (S6) and (S7) are the hydrodynamic equations that describe the spatial-temporal dynamics of the electron velocity and density. In above equations, $\boldsymbol{E}$ and $\boldsymbol{H}$ are the electric and magnetic fields interacting with the system, $\boldsymbol{P}$ is the polarization vector, e, m_e, γ, n, and $\boldsymbol{v}$ are the electron charge, mass, collision frequency, density, and velocity, respectively, p represents the quantum pressure giving rise to the nonlocal response. In the framework of the multi-physical model, the Maxwell's and the hydrodynamic equations are coupled via the polarization term $\partial_t \boldsymbol{P} = -ne\boldsymbol{v}$, in which the linear, nonlinear, and broadband chromatic dispersion are included. In this work, the sets of Eqs. (S4) to (S7) were rigorously solved by the FDTD method, which helps reveal the mechanism of the enhanced THz generation from the SRR-ITO metasurface.

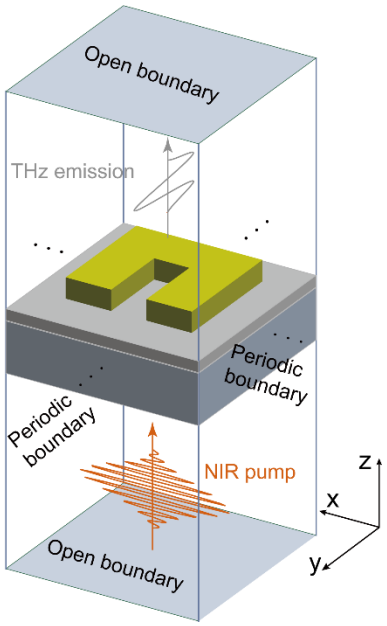

Figure S6. Schematic of the FDTD simulation setup for the uniform metasurface.

The simulations were based on an in-house FDTD solver. To efficiently solve the multi-physical equations, we adapt the FDTD solver to a multiple graphical processing unit environment using the NVIDIA® Compute Unified Device Architecture (CUDA) technique. As sketched in Figure S6, a metasurface unit cell was illuminated by a plane wave propagating along the *z*-axis in the simulation. The plane wave source was introduced using the total-field and scattered-field (TF/SF) technique. Open scattering boundaries were employed at the *z* directions, and periodic boundaries were employed at the *x* and *y* directions. The spatial and temporal steps were $\Delta x = \Delta y = \Delta z = 1\times 10^{-9}$ m and $\Delta t = 1.5 \times 10^{-18}$ s for convergence.

Both gold and ITO are considered as plasmonic materials that can be quantitatively described by a Drude model[4], $\varepsilon_{ITO}(\omega) = \varepsilon'(\omega) - i\varepsilon''(\omega) = \varepsilon_\infty - \omega_p^2/(\omega^2 + i\omega\gamma)$, where ε_∞ is the infinite frequency permittivity, $\omega_p = \sqrt{ne^2/(\varepsilon_0 m)}$ is the plasma frequency determined by the carrier density n, and γ is the collision frequency. For gold, these parameters were set as $\varepsilon_\infty = 1$, $\omega_p = 1.366$

$\times 10^{16}$ rad s^{-1}, and $\gamma = 1.2 \times 10^{14}$ rad s^{-1}. For the ITO, these parameters were set as $\varepsilon_\infty = 4.1$, $\omega_p = 2.7297 \times 10^{15}$ rad s^{-1}, and $\gamma = 2.9326 \times 10^{14}$ rad s^{-1}. In this model, the ENZ wavelength of the ITO film is given by $\lambda_{ENZ} = 2\pi c \Big/ \sqrt{\omega_p^2 / \varepsilon_\infty - \gamma^2} = 1432$ nm.

4.2. *The mechanism of the enhanced THz generation*

Figure S7a,b show the simulated fundamental near-field distributions ($|E_{FW,z}|$) of the SRR and SRR-ITO meta-atoms under *x*-polarized illumination at normal incidence, respectively. For the SRR metasurface illuminated by a FW at 1400 nm wavelength, linear field enhancement takes place on the surface of the SRR due to the plasmonic resonance (see Figure S7a). However, much stronger field enhancement is observed near the SRR-ITO interface (see Figure S7b) for the SRR-ITO metasurface illuminated by a FW at 1350 nm wavelength due to the coupling effect. Without loss of generality, the corresponding simulated nonlinear THz near-field distributions ($|E_{THz,y}|$) of the two meta-atoms at 2.0 THz are shown in Figure S7c,d. It is observed that the THz electric field primarily confined in the vicinity of the SRR-ITO interface (see Figure S7d) is much larger than that at the gap of the SRR in the absence of the ITO film (see Figure S7c). Figure S7e,f show the simulated distributions of the nonlinear THz charge densities and currents of the two meta-atoms at 2.0 THz. Due to the magnetic dipole resonance, both SRRs possess the same nonlinear dynamics, i.e. nonlinear currents in arms are parallel along the *y*-direction but canceled in the *x*-direction, resulting in generation of *y*-polarized THz signal. However, the charges are mainly accumulated on the ITO surface rather than in the SRR, which indicates that the enhanced THz generation mainly occurs in the ITO layer, as shown in Figure S7f.

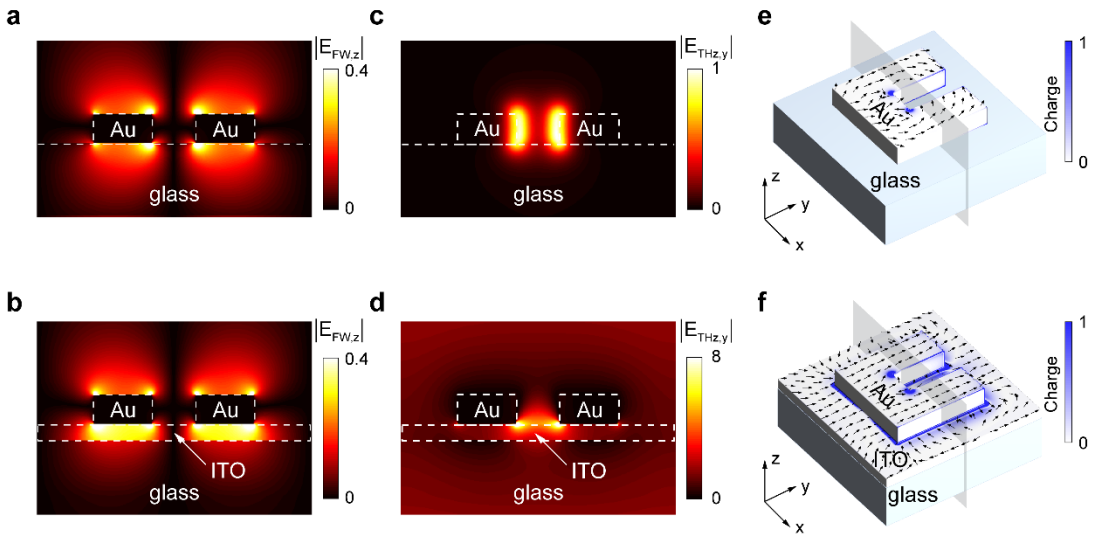

Figure S7. (a,b) Simulated $|E_{FW,z}|$ near-field distributions of the meta-atoms of the SRR and SRR-ITO metasurfaces, respectively. (c,d) Simulated $|E_{THz,y}|$ near-field distributions of the meta-atoms of the SRR and SRR-ITO metasurfaces at 2.0 THz, respectively. (e,f) Simulated normalized THz charge density (color) and current (arrows) distributions of the meta-atoms of the SRR and SRR-ITO metasurfaces at 2.0 THz, respectively. All results are obtained under normal illumination with *x*-polarized FWs. For the SRR and SRR-ITO metasurfaces, the fundamental near-field distributions in (a,b) are plotted at pump wavelengths of 1400 nm and 1350 nm, respectively. The results in (a-d) are plotted for the *xz* cross sections marked by translucent planes in (e,f).

4.3. *The role of mode coupling in the enhanced THz generation*

In the SRR-ITO metasurface, though the nonlinearity of the SRR makes an insignificant contribution to the THz generation as demonstrated above, the mode coupling between the magnetic dipole mode of the SRR and the ENZ mode of the ITO layer plays an important role. To reveal the role of the mode coupling, a SiO_2 spacer was sandwiched between the SRR and the ITO film, in which the mode coupling strength is tuned by changing the interlayer thickness. Figure S8a shows the simulated transmission spectra of the SRR-SiO_2-ITO metasurfaces with different

SiO_2 thicknesses at normal incidence. As the SiO_2 thickness increases, the coupling strength between the SRR and the ITO film becomes weaker.

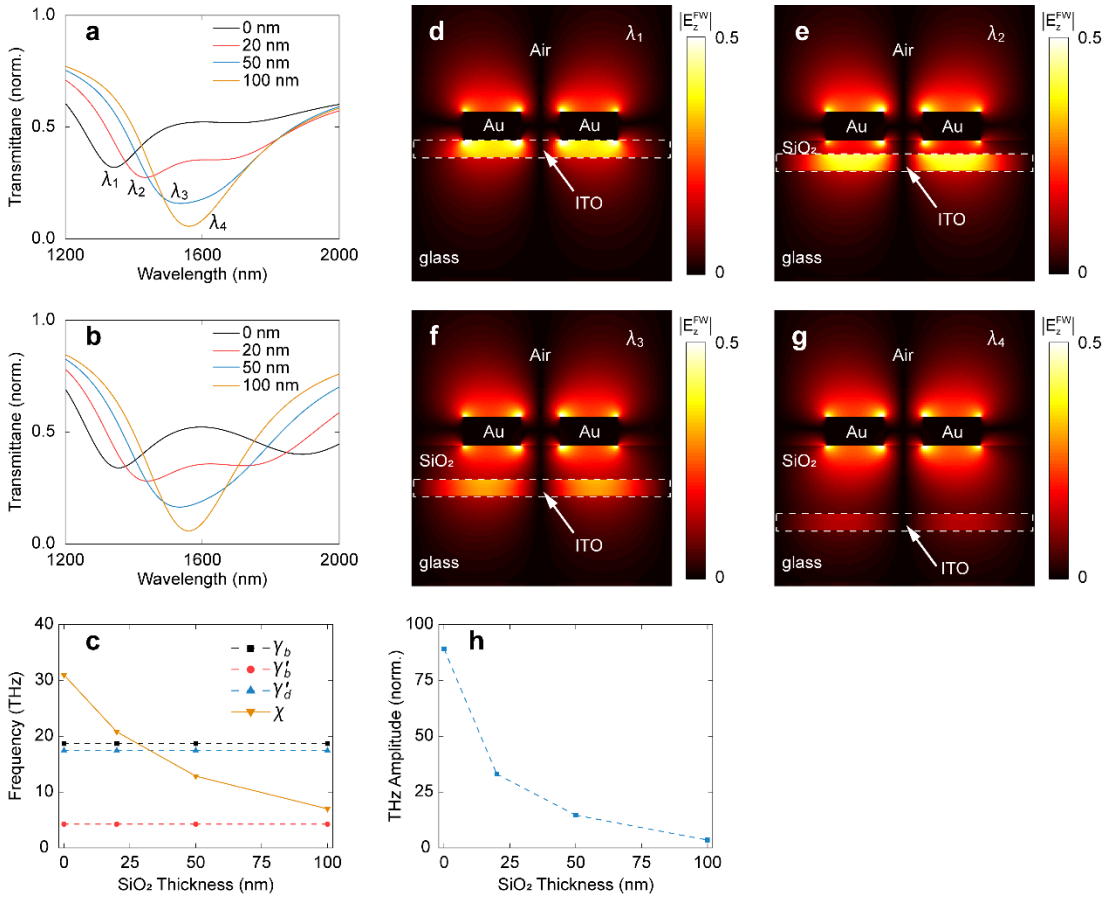

Figure S8. (a,b) Simulated and fitted transmission spectra of the SRR-SiO_2-ITO metasurfaces with SiO_2 spacer thicknesses of 0, 20, 50, and 100 nm, respectively. (c) Corresponding fitted parameters with respect to the thickness of SiO_2 in CMT. (d-g) Simulated absolute fundamental *z*-component electric field distributions of the SRR-SiO_2-ITO metasurfaces with respect to (a) at wavelengths of λ_1 = 1276 nm, λ_2 = 1363 nm, λ_3 = 1469 nm, and λ_4 = 1485 nm, respectively. These results are all normalized to the maximum electric field of (d). (h) Simulated maximum THz peak-to-peak amplitudes generated from the SRR-SiO_2-ITO metasurfaces with respect to (a). They are all normalized to the THz peak-to-peak amplitude generated from the SRR metasurface.

Figure S8b illustrates the fitted transmission results using Eq. (S3), which reasonably agrees with the simulated results. The corresponding fitted parameters are shown in Figure S8c. To reveal the influence of the coupling effect, we only adjusted the coupling coefficient in the fitting. It is clearly seen that the main features and trends of the fitting results agree well with the simulated results, where the coupling coefficient indeed gradually decreases as expected. Figure S8d-g illustrate the simulated fundamental *z*-component electric field distributions. The field strength in the ITO film coupled with the resonant SRR decreases as the SiO_2 thickness increases. This results in the dramatic decrease of the generated THz signals, as shown by the corresponding simulated THz peak-to-peak amplitudes in Figure S8h.

4.4. *Simulated pump-wavelength-dependent THz generation*

With this simulation technique, we also calculate the pump-wavelength-dependent THz peak-to-peak amplitudes of the SRR-ITO metasurface and the SRR metasurface. In this nonlinear simulation, the pump laser was described by a Gaussian pulse $E(t) = E_0\exp[-(2\ln 2)\,(t - t_0)^2/\tau^2]\cos(\omega_0 t)$, where the temporal pulse width, the peak amplitude, and the wavelength of the incident fundamental wave were set as τ = 60 fs, $E_0 = 7 \times 10^7$ V m^{-1}, $\lambda_0 = 2\pi c/\omega_0 \in$ [1200 nm, 2000 nm] according to the experimental parameters, respectively. The pump laser illuminates the metasurfaces at normal incidence with polarization perpendicular to the gap of the SRR (along *x*). Figure S9 illustrates the simulated pump-wavelength-dependent THz peak-to-peak amplitudes generated by the SRR-ITO metasurface and the SRR metasurface, respectively. The amplitude maxima nearly coincide with the corresponding resonance wavelengths. For the SRR-ITO

metasurface, the THz amplitude achieved by pumping at the shorter resonance wavelength is much larger than that achieved by pumping at the longer resonance wavelength. The THz amplitude maximum for pumping the SRR-ITO metasurface at 1306 nm is ~90 times larger than that of the SRR metasurface for pumping at 1390 nm. All these simulated nonlinear features of the THz generation agree well with the measured results in Figure 2e.

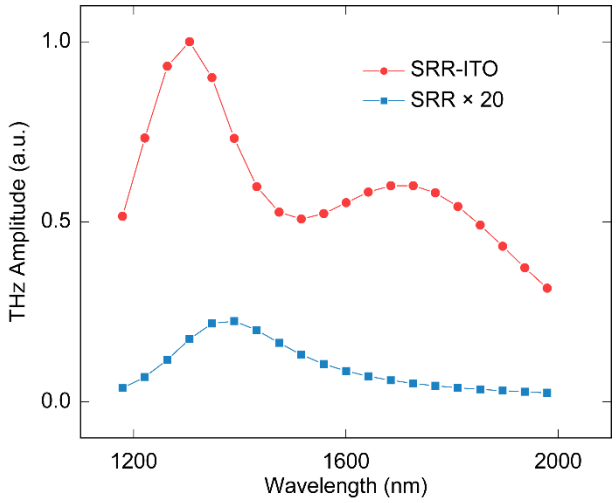

Figure S9. Simulated pump-wavelength-dependent THz peak-to-peak amplitudes generated by the SRR-ITO metasurface and the SRR metasurface.

Note 5. Derivation of the nonlinear PB phase for the THz emission

As shown in Figure 3a, a circularly polarized fundamental wave illuminates an SRR along the +z direction. The incident field $\mathbf{E}_{\mathrm{FW}}$ can be expressed using the Jones vector

$$\mathbf{E}_{\mathrm{FW}} = \frac{1}{\sqrt{2}}\begin{bmatrix} 1 \\ \sigma i \end{bmatrix} \tag{S8}$$

in the laboratory x-y coordinates, where $\sigma = +1/-1$ corresponds to the left-/right-handed circularly polarized (LCP/RCP) field, respectively. For the SRR with zero rotation angle, i.e. $\theta = 0°$, the emitted THz nonlinear polarization can be defined as:

$$\mathbf{P}_{\mathrm{THz},0} = \varepsilon_0 \vec{\chi}^{(2)}_{\mathrm{eff}} \mathbf{E}_{\mathrm{FW},1} \mathbf{E}^{*}_{\mathrm{FW},2}, \tag{S9}$$

where $\vec{\chi}^{(2)}_{\mathrm{eff}}$ represents the effective nonlinear susceptibility tensor regarding the optical rectification effect. When $\theta \neq 0$, Eq. (S9) should be applied in the local x'-y' coordinate, as shown in Figure 3a. In this x'-y' coordinate, the incident field $\mathbf{E}'_{\mathrm{FW}}$ is given by

$$\mathbf{E}'_{\mathrm{FW}} = \mathbf{\Theta}\mathbf{E}_{\mathrm{FW}} = \frac{1}{\sqrt{2}}\begin{bmatrix} \cos\theta & -\sin\theta \\ \sin\theta & \cos\theta \end{bmatrix}\begin{bmatrix} 1 \\ \sigma i \end{bmatrix} = \frac{\mathrm{e}^{i(-\sigma\theta)}}{\sqrt{2}}\begin{bmatrix} 1 \\ \sigma i \end{bmatrix} = \mathrm{e}^{i(-\sigma\theta)} \cdot \mathbf{E}_{\mathrm{FW}}, \tag{S10}$$

where $\mathbf{\Theta}$ is the rotation matrix from x-y coordinate to x'-y' coordinate. Therefore, the THz nonlinear polarization of the rotated SRR in the x'-y' coordinate can be expressed as

$$\mathbf{P}'_{\mathrm{THz},0} = \varepsilon_0 \vec{\chi}^{(2)}_{\mathrm{eff}} \mathbf{E}'_{\mathrm{FW},1} \left(\mathbf{E}'_{\mathrm{FW},2}\right)^{*} = \varepsilon_0 \vec{\chi}^{(2)}_{\mathrm{eff}} \left[\mathrm{e}^{i(-\sigma\theta)} \cdot \mathbf{E}_{\mathrm{FW},1}\right]\left[\mathrm{e}^{i(-\sigma\theta)} \cdot \mathbf{E}_{\mathrm{FW},2}\right]^{*} = \mathbf{P}_{\mathrm{THz},0}, \tag{S11}$$

Next, we decompose the above THz nonlinear polarization in the circular polarization basis as

$$\mathbf{P}'_{\mathrm{THz},0} = \mathrm{P}^{\mathrm{LCP}}_{\mathrm{THz},0}\begin{bmatrix} 1 \\ i \end{bmatrix} + \mathrm{P}^{\mathrm{RCP}}_{\mathrm{THz},0}\begin{bmatrix} 1 \\ -i \end{bmatrix}, \tag{S12}$$

where $\mathrm{P}^{\mathrm{LCP}}_{\mathrm{THz},0}$ and $\mathrm{P}^{\mathrm{RCP}}_{\mathrm{THz},0}$ represent the amplitude of the LCP and RCP components, respectively. At last, Eq. (S12) should be applied back to the x-y coordinate as

$$\mathbf{P}_{\mathrm{THz},\theta} = \mathbf{\Theta}^{-1}\mathbf{P}'_{\mathrm{THz},0} = \mathrm{e}^{i\theta}\cdot P^{\mathrm{LCP}}_{\mathrm{THz},0}\begin{bmatrix}1\\ i\end{bmatrix} + \mathrm{e}^{i(-\theta)}\cdot P^{\mathrm{RCP}}_{\mathrm{THz},0}\begin{bmatrix}1\\ -i\end{bmatrix}. \tag{S13}$$

It can be seen that σ disappears in the phase terms in Eq. (S13), which means that the phases of the THz nonlinear polarizations do not depend on the handedness of the incident circularly polarized field as in the harmonic generation cases. Indeed, the THz radiation should be expected to be independent of the handedness of the CP pump beam considering that the infrared pump pulse oscillates around 100× faster than the THz pulse. Compared to the timescale of a THz oscillation, the IR excitation of all SRR orientations occurs simultaneously, regardless of the handedness of the IR pump pulse, and may thus be expected to generated the same THz field for LCP and RCP pump pulses. According to Eq. (S13), the emitted LCP and RCP THz waves from an SRR with a rotation angle of θ acquire nonlinear PB phases of θ and $-\theta$, respectively:

$$E^{\mathrm{LCP}}_{\mathrm{THz}} \propto \mathrm{e}^{i\theta}, \tag{S14}$$

$$E^{\mathrm{RCP}}_{\mathrm{THz}} \propto \mathrm{e}^{i(-\theta)}. \tag{S15}$$

Moreover, the above derivation does not involve any dispersion effect, which means that any optical rectification effect that contributes to the THz generation will acquire the same nonlinear PB phase. Therefore, the nonlinear PB phase here is naturally broadband.

References

(1) Huang, W. X.; Lin, J.; Qiu, M.; Liu, T.; He, Q.; Xiao, S. Y.; Zhou, L. A complete phase diagram for dark-bright coupled plasmonic systems: applicability of Fano's formula. *Nanophotonics* **2020**, 9, 3251-3262.

(2) Planken, P. C. M.; Nienhuys, H. K.; Bakker, H. J.; Wenckebach, T. Measurement and calculation of the orientation dependence of terahertz pulse detection in ZnTe. *J. Opt. Soc. Am. B* **2001**, 18, 313-317.

(3) van der Valk, N. C. J.; Wenckebach, T.; Planken, P. C. M. Full mathematical description of electro-optic detection in optically isotropic crystals. *J. Opt. Soc. Am. B* **2004**, 21, 622-631.

(4) Reshef, O.; De Leon, I.; Alam, M. Z.; Boyd, R. W. Nonlinear optical effects in epsilon-near-zero media. *Nat. Rev. Mater.* **2019**, 4, 535-551.